

3D BENDING OF SURFACES AND VOLUMES WITH AN APPLICATION TO BRAIN TORQUE MODELING

Antonietta Pepe^{1*}, Jussi Tohka¹

¹*Department of Signal Processing, Tampere University of Technology,
P.O. Box 553, FIN-33101 Tampere, Finland
{antonietta.pepe, jussi.tohka}@tut.fi*

Keywords: Space deformation; 3D surfaces and volumes bending; Brain asymmetry; Magnetic resonance imaging.

Abstract: In this work, we propose a novel space deformation model for local bending of 3D volumes and surfaces. The model can be easily controlled through accommodation of a few intuitive parameters. Experiments on volumes, parametric surfaces, and polygonal surfaces show that our method has increased modeling capabilities when compared to the previous space deformation methods for local bending. We apply this new, more flexible model for space bending to model human brain asymmetry. In particular, we develop an image processing pipeline for automatic generation of a set of realistic 3D brain magnetic resonance (MR) images for which the asymmetry is known. This dataset can be used for the quantitative validation of voxel and surface based methods for studying brain shape asymmetry. The pipeline encompasses a realistic modeling of the anatomical rightward bending of the inter-hemispheric fissure in human brain.

1 INTRODUCTION

Space Deformation (SD) methods are efficient and intuitive class of methods for deforming multidimensional shapes. In SD methods, the object's shape is modified by deforming the underlying space in which the object is embedded regardless of the particular shape representation employed. Besides the scaling, translation, rotation and affine transformations, more sophisticated parametric remappings of the space (e.g. the global linear bending) have been proposed (Barr, 1984).

Free Form Deformation (FFD) methods (Sederberg and Parry, 1990) are another class of shape morphing techniques that enable the deformation of geometric models through deformations of the underlying space. In FFD techniques, the object to be deformed is first embedded in a lattice. Control points of the lattice are then moved to control the space deformation.

Even though FFD methods can express a larger number of deformations than SD methods, there are still some advantages in using SD. First, the control lattice used to deform the space in FFD is not directly related to the coordinates of the object being deformed. Due to this indirect framework, controlling the deformation requires expertise. Second, SD provides a more compact way to encode the deformations if compared to the high number of control points which are required in FFD. Related to this, moving the control

points can be time consuming (Xiaogang et al., 2001; Hsu, 1992).

In this work, we used SD based methods for modeling of the bending deformation. The main contributions of this work can be summarized as follows:

1) We extended the linear bending deformation proposed in (Barr, 1984) to allow more flexible transformations of the space, as well as to include constraints on the deformation while maintaining the simplicity of the model. The usefulness of the proposed bending deformations, in terms of increased modeling power, is demonstrated in this work.

2) The two most consistently reported patterns of normal asymmetry in the human brain anatomy are the protrusion of one hemisphere over the other at the frontal and occipital lobes (petalia), and the rightward bending of the inter-hemispheric fissure (known as brain torque or Yakovlevian anti-clockwise torque) due to the protrusion of the left hemisphere over the right one in the occipital region (Toga and Thompson, 2003). In this work, we develop a realistic model of the left occipital right frontal petalia and of the brain torque deformations. The proposed model is suitable for any brain shape representation.

3) There exist automatic methods for the statical shape analysis of the anatomical asymmetries in the human brain based on 3D magnetic resonance (MR) images. In such methods, the brain shape asymmetry

can be either analyzed through morphometric voxel level measures computed from flipped and unflipped MR images (Voxel Based Morphometry) (Ashburner and Friston, 2000; Good et al., 2001), or through measures computed along a surface mesh representation of the cerebral hemispheres at corresponding locations on the two sides of the brain (Surface Based Morphometry) (Thompson et al., 1997; Pepe et al., 2011). In this work, we have developed an automatic image processing pipeline for the generation of validation databases for voxel and surface based methods for the analysis of brain shape asymmetry from 3D MR images.

2 BACKGROUND

Space Deformations SD techniques modify the shape of objects by deforming the space in which they are embedded. The space deformation can either be applied to the whole space, $S = \mathcal{F}(s)$, or defined locally, $\mathbf{J}_i(s) = \partial \mathcal{F}(s) / \partial s_i$ (Barr, 1984; Sumner, 2005). In the above expressions $\mathcal{F} : \mathbb{R}^n \rightarrow \mathbb{R}^n$ denotes the global transformation function, \mathbf{J} denotes the Jacobian matrix of the transformation \mathcal{F} , s denotes the object embedded in the space operated by \mathcal{F} , and S denotes the resulting deformed object.

Often, it is useful to calculate the normal and tangent vectors of the deformed object S . These can be used to obtain the surface's orientation, to derive the reflectivity of a light source onto a surface for lighting, to add details to a surface, e.g., roughness to a flat surface, and for surface interpolation (shading). The computation of normal and tangent vectors can be a computationally intensive task¹, especially for polygonal meshes having thousands of vertices. However, the tangent t^S of the deformed object S can be computed directly from the tangent normal of the undeformed object (t^s) through a simple matrix multiplication by the Jacobian of the deformation: $t^S = \mathbf{J}t^s$ (Barr, 1984). Similarly, the normal vector n^S of the deformed object S can be computed as proportional to the inverse transpose of the Jacobian

¹For a parametric surface $s = s(u, v)$, the tangent vector t^s can be computed as the linear combination of the partial derivatives of s with respect to the two variables u and v ; whereas the normal vector n^s can be computed as the cross product of two linearly independent tangent vectors. Similarly, the normal vector at a face on a surface mesh s can be calculated as the cross product of two linearly independent tangent vectors at that face, while the normal vector at a vertex on the surface mesh is equal to the normalized sum of the normals in each face connected to the vertex (3 in case of triangulated surface meshes).

matrix times the normal vector of the undeformed object: $n^S = \det(\mathbf{J})\mathbf{J}^{-1T}n^s$ (Barr, 1984). Such tangent and normal transformation rules allow a fast calculation of the tangent and normal vectors, increasing the practical usefulness of SD methods for geometry modeling and surface morphing applications.

Global Linear Bending A model for the isotropic Global Linear Bending (GLB) deformation was first introduced in (Barr, 1984). In GLB, the space is bended along a line parallel to one of the axis by a piece-wise constant deformation. More in detail, in the bending region, the bending deformation is approximated through simultaneous rotations and translations of two components of each point around the third one. In the non bending regions, the space is rigidly rotated and translated. In the following sections, we propose modifications to the GLB model named as modified GLB (mGLB), adaptive modified GLB (amGLB), and rescaled adaptive modified GLB (ramGLB).

3 DEFORMATION MODELS

3.1 Modified Global Linear Bending

Let (x, y, z) and (X_m, Y_m, Z_m) denote the original (undeformed) and deformed x , y and z coordinates, respectively. The modified Global Linear Bending (mGLB) along a centerline parallel to the y axis is defined as follows (bending along lines parallel to the x and z axes are obtained in the same way as for the y axis):

$$X_m = \begin{cases} C_\theta(x - \frac{1}{k_1}) + \frac{1}{k_1} + S_\theta(y - y_A) & \text{if } y < y_A \\ C_\theta(x - \frac{1}{k_1}) + \frac{1}{k_1} & \text{if } y_A \leq y < y_1 \\ C_\theta(x - \frac{1}{k_1}) + \frac{1}{k_1} + S_\theta(y - y_1) & \text{if } y_1 \leq y \leq y_2 \\ C_\theta(x - \frac{1}{k_2}) + \frac{1}{k_2} & \text{if } y_2 < y \leq y_C \\ C_\theta(x - \frac{1}{k_2}) + \frac{1}{k_2} + S_\theta(y - y_C) & \text{if } y > y_C \end{cases} \quad (1)$$

$$Y_m = \tilde{Y}_m + \tilde{y}_m =$$

$$= \begin{cases} -S_\theta(x - \frac{1}{k_1}) + C_\theta(y - y_A) + y_1 & \text{if } y < y_A \\ -S_\theta(x - \frac{1}{k_1}) + y_1 & \text{if } y_A \leq y < y_1 \\ -S_\theta(x - \frac{1}{k_1}) + C_\theta(y - y_1) + y_1 & \text{if } y_1 \leq y \leq y_2 \\ -S_\theta(x - \frac{1}{k_2}) + y_2 & \text{if } y_2 < y \leq y_C \\ -S_\theta(x - \frac{1}{k_2}) + C_\theta(y - y_C) + y_2 & \text{if } y > y_C \end{cases} \quad (2)$$

$$Z_m = z \quad (3)$$

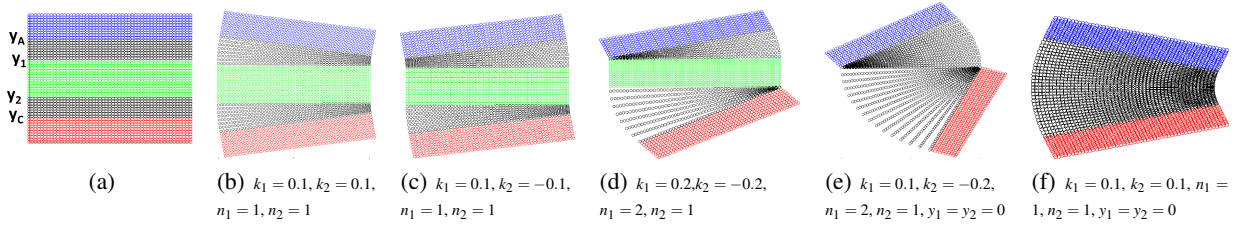


Figure 1: The modified Global Linear Bending (mGLB) deformation. A space $(x, y) \in [-5, 5] \times [-5, 5]$ with bending region defined by $y_A = -3, y_1 = -1.5, y_2 = 1.5$, and $y_C = 3$ (a) is remapped in (b)-(d) using the mGLB with varying values for k_1, k_2, n_1 , and n_2 . Undeformed and deformed spaces are depicted in 2D as the mGLB deformation around the y axis (as defined by Eq. 1-4) is constant along the z axis. Panels (b)-(e) show that the space deformations in the two bending regions (depicted in black color) can have different directions and intensities. Panel (f) shows one of the 3 possible cases when the mGLB reduces to the GLB space deformation.

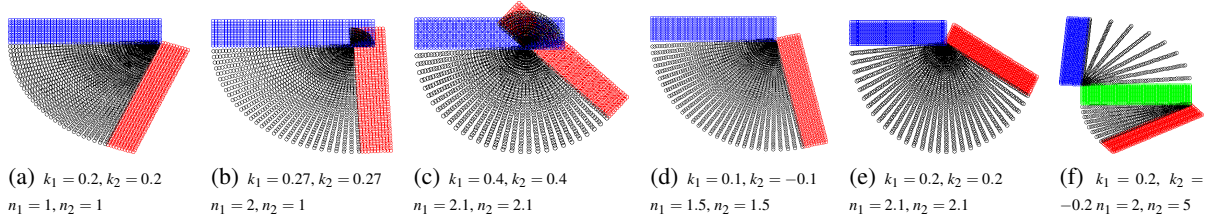


Figure 2: The effects of the factors of bending amplification on mGLB space deformation. Panels (a)-(e) show a space $(x, y) \in [-5, 5] \times [-5, 5]$ deformed by mGLB with $y_A = -3, y_1 = y_2 = 0, y_C = 3$, and with varying values for $k_1 = k_2$ and $n_1 = n_2$. The mGLB remappings depicted in panels (a)-(c) reduce to the original GLB deformation. A crimp effect can be seen in the top right most part of (b) and (c). The mGLB space deformations depicted in panels (d) and (e) produce similar amount of bending as in (b)-(c), but with no crimp effect. In (f), a more general example of mGLB space deformation with a relatively high level of bending and no crimp effect is depicted.

where:

$$\theta = \begin{cases} n_1 k_1 (y_A - y_1) & \text{if } y < y_A \\ n_1 k_1 (y - y_1) & \text{if } y_A \leq y < y_1 \\ 0, & \text{if } y_1 \leq y \leq y_2 \\ n_2 k_2 (y - y_2) & \text{if } y_2 < y \leq y_C \\ n_2 k_2 (y_C - y_2) & \text{if } y > y_C \end{cases} \quad (4)$$

In above, θ is the bending angle; y_1 and y_2 are the centers of the deformations; k_1 and k_2 are the constant bending rates measured in radians per unit length; n_1 and n_2 are the constants factors of bending amplification; and C_θ and S_θ are defined as $\cos(\theta)$ and $\sin(\theta)$, respectively. Parameters y_A, y_1, y_2 and y_C define the bending regions.

In the non bending regions $y \in (\infty, y_A)$ and $y \in (y_C, \infty)$, the mGLB deformation consists of rigid body translations and rotations with a constant angle θ . The non bending region $y \in [y_1, y_2]$ remains unaffected by the mGLB transformation as $\theta = 0$. In the bending regions $y \in [y_A, y_1]$ and $y \in [y_2, y_C]$, θ changes linearly with y , and the bending deformations are approximated through simultaneous rotations and translations of two components of each point around the third one. The mGLB model is C^0 continuous as the deformed X_m, Y_m , and Z_m functions have continuous values along y but their derivatives with respect to y are not

continuous at regions' boundaries.

If $y_1 = y_C$ and $n_1 = 1$; or if $y_2 = y_A$ and $n_2 = 1$; or if $y_1 = y_2$ and $n_1 = n_2 = 1$ and $k_1 = k_2$, then the mGLB reduces to the original GLB deformation in (Barr, 1984). The mGLB deformation is a generalization of the GLB deformation in following two aspects.

1) Whereas in GLB there were two non-bending and one bending regions, the mGLB deformation in Eq. 1-4 is composed of three non bending regions: $y \in (\infty, y_A)$, $y \in (y_C, \infty)$, and $y \in [y_1, y_2]$; and two bending regions: $y \in [y_A, y_1]$ and $y \in [y_2, y_C]$. Moreover, the bending rates k_1 and k_2 and the factors of bending amplification n_1 and n_2 in the mGLB deformation can have different signs and values, and thus the direction and intensity of the deformation can be different in the two bending regions (see Fig. 1.(b)-(d)). Due to this, the mGLB deformation can model a number of phenomena not otherwise possible through GLB, e.g, the brain torque.

2) The second novelty of the mGLB is the addition of the multiplicative factors $n_i, i = 1, 2$ to the definition of the bending angle θ . If $|n_i| > 1$, the degree of bending increases by a factor $|n_i|$ through amplification of the angles spanned by the mGLB in the bending regions ($[y_A, y_1]$ if $i = 1$, $[y_2, y_C]$ if $i = 2$). Negative values of n_i result in a swap of the direction of the bending with respect to the one expressed by the sign

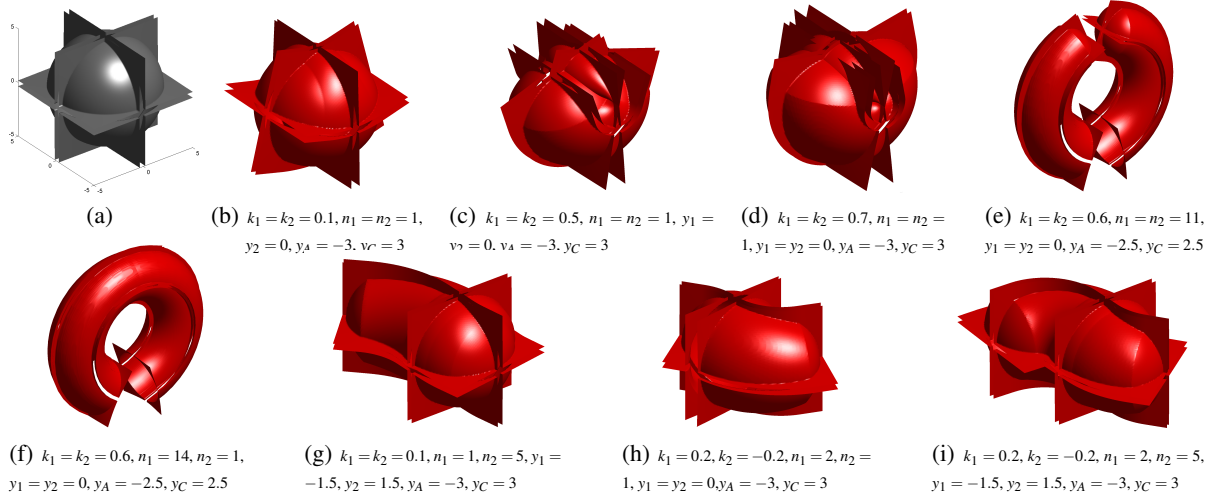


Figure 3: Examples of shapes deformed by the modified Global Linear Bending (mGLB) deformation. (a) A parametric surface (a sphere - $|x|^2 + |y|^2 + |z|^2 = 1$ - with a cross inside) is embedded in a 3D space $(x, y, z) \in [-5, 5] \times [-5, 5] \times [-5, 5]$, and then deformed (b)-(i) by the mGLB with varying values of the model parameters. Panels (b)-(d) show examples of objects deformed by the original GLB with increasing bending rates. A crimp effect can be observed for high degrees of the bending in panels (c) and (d) but not in the case of mGLB in panels (e) and (f). Panels (g)-(i) show surface deformed by the mGLB space deformation with $k_1 n_1 \neq k_2 n_2$: different directions and/or intensities of the deformations in the two bending regions.

Table 1: The normal and tangent rules, and the rates of local volumetric change for the mGLB space deformation.

\mathbf{J}	\mathbf{J}^{-1T}	$\det(\mathbf{J})$	$\hat{\mathbf{k}}$	$\hat{\mathbf{n}}$
$\begin{pmatrix} C_\theta & S_\theta(1-\hat{k}x)\hat{n} & 0 \\ -S_\theta & C_\theta(1-\hat{k}x)\hat{n} & 0 \\ 0 & 0 & 1 \end{pmatrix}$	$\begin{pmatrix} C_\theta(1-\hat{k}x)\hat{n} & S_\theta & 0 \\ -S_\theta(1-\hat{k}x)\hat{n} & C_\theta & 0 \\ 0 & 0 & (1-\hat{k}x)n \end{pmatrix}$	$(1-\hat{k}x)n$	$\begin{cases} k_1 & \text{if } y_A \leq y < y_1 \\ k_2 & \text{if } y_2 \leq y < y_C \\ 0 & \text{otherwise} \end{cases}$	$\begin{cases} n_1 & \text{if } y < y_2 \\ n_2 & \text{if } y \geq y_2 \end{cases}$

of k_i . This bending angle amplification helps to avoid the crimp effect as is illustrated in Fig. 2 in the simplified case of $y_1 = y_A$, $y_2 = y_C$ and $k_1 = k_2$. Particularly, in Fig. 2.(a)-(c), three examples of the mGLB deformations that reduce to GLB deformations with increasing values of $k_1 = k_2$ (and constant values of y_A, y_C and $n_1 = n_2 = 1$) are shown. A crimp effect, consisting of an overlap in the deformed portions of the grid in the bending and non bending regions, can be seen in the top right most parts of Fig. 2.(b) and (c). This crimp effect, also described in (Barr, 1984), increases as $|k_i|$ increases. However, in many practical situations, it is necessary to model a relatively high degree of bending and still avoid the crimp effect as that could result in unrealistic deformations (Fig. 3.(c) and (d)). This is especially true if the objects occupy a relatively large volume of the space being deformed. In Fig. 2.(d)-(e), we show how a proper tuning of the pair (k_i, n_i) can be used to produce high degree of bending and still avoid the crimp effect (see also Fig. 3.(e) and (i)). The rule of thumb is to fix $n_i = 1$ and choose the maximum value of k_i (\hat{k}) not producing the crimp effect; then, for a fixed $k_i = \hat{k}_1$, to increase n_i until the desired level of bend-

ing is achieved. In principle, any degree of bending with no crimp effect can be achieved using the mGLB deformation.

The mGLB space transformations were used to deform a few parametric surfaces in Fig. 3. Note how the addition of a few parameters to the model resulted in remarkably more ductile and realistic deformations.

The expressions for the Jacobian matrix (\mathbf{J}), its inverse transpose (\mathbf{J}^{-1T}), and its determinant ($\det(\mathbf{J})$) for the mGLB deformations are given in 1. The above quantities are needed, respectively, for the tangent and normal transformation rules, and to calculate the rate of local volumetric change introduced by the proposed deformation.

3.2 Adaptive Modified Global Linear Bending

Even though the mGLB deformation would in principle enable the simultaneous leftward and rightward bending of the inter-hemispheric fissure at the frontal and occipital lobes, respectively, fine adjustments of the mGLB are needed to better model this pattern of structural asymmetry of the human brain. More

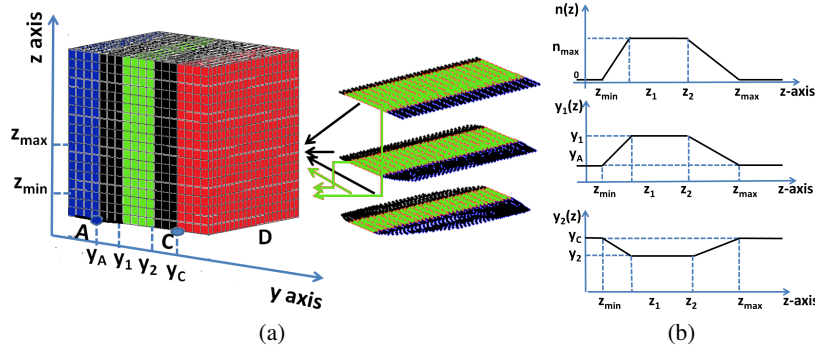


Figure 4: The adaptive modified Global Linear Bending (amGLB). (a) Different space deformations applied at different $z \in [z_{min}, z_{max}]$; and (b) definition of the model parameters $n_1(z)$, $n_2(z)$, $y_1(z)$, and $y_2(z)$. In the transition area between the cerebellum and the lower portions of the cerebrum (when $z > z_{min}$), the bending amplification $n_1(z), n_2(z)$ is increased gradually while the bending regions $([y_A, y_1(z)])$ and $(y_2(z), y_C]$ become gradually narrower. Viceversa in the transition area between the lower and higher portions of the cerebrum.

specifically, the bending of the cerebral hemispheres is localized in the most inferior part (i.e. the part with a small z -coordinate) of the cerebrum. Thus, we apply a mGLB style deformation only when $z_{min} \leq z \leq z_{max}$. This way, it is possible to deform the bottom part of the cerebrum while leaving the cerebellum ($z < z_{min}$) and the upper portions of the cerebrum ($z > z_{max}$) undeformed. To obtain smooth transitions between the deformed ($z_{min} \leq z \leq z_{max}$) and undeformed ($z < z_{min}$, $z > z_{max}$) regions along the z axis, the adaptive modified Global Linear Bending (amGLB) model is designed to enable scalable levels of the mGLB style space deformations.

The amGLB deformation along a line parallel to the y axis is defined as the mGLB space deformation in Eqs. (1)-(4), but the factors of bending amplifications, n_1 and n_2 , and the parameters y_1 and y_2 , are the following functions of z -coordinate:

$$\hat{n}_i(z) = \begin{cases} \frac{n_{max}}{z_1 - z_{min}}(z - z_{min}) & \text{if } z_{min} < z < z_1 \\ \frac{n_{max}}{z_2 - z_{max}}(z - z_{max}) & \text{if } z_2 < z < z_{max} \\ n_{max} & \text{if } z_1 \leq z \leq z_2 \\ 0 & \text{otherwise} \end{cases} \quad (5)$$

$$\hat{y}_1(z) = \begin{cases} \frac{y_1 - y_A}{z_1 - z_{min}}(z - z_{min}) + y_A & \text{if } z_{min} < z < z_1 \\ \frac{y_1 - y_A}{z_2 - z_{max}}(z - z_{max}) + y_A & \text{if } z_2 < z < z_{max} \\ y_1 & \text{if } z_1 \leq z \leq z_2 \\ y_A & \text{otherwise} \end{cases} \quad (6)$$

$$\hat{y}_2(z) = \begin{cases} \frac{y_2 - y_C}{z_1 - z_{min}}(z - z_{min}) + y_C & \text{if } z_{min} < z < z_1 \\ \frac{y_2 - y_C}{z_2 - z_{max}}(z - z_{max}) + y_C & \text{if } z_2 < z < z_{max} \\ y_2 & \text{if } z_1 \leq z \leq z_2 \\ y_C & \text{otherwise} \end{cases} \quad (7)$$

where $i = 1, 2$; y_1 and y_2 are parameters for the centers of the deformation; $z_{min} \leq z_1 \leq z_2 \leq z_{max}$ and n_{max} are model parameters. See Fig. 4 for an illustration.

The amGLB deformation introduces local changes on the size of the deformed space. In fact, while the protrusions of the left occipital and the right frontal lobes, thus the local volumetric changes, at the interhemispheric region are desirable, the total volume of the brain should not change. In the same way, the shape and position of the skull and scalp regions should not be modified by the space deformation. To prevent this, we added to the model a rescaling factor in the x ($r_x(z)$) the ($r_y(z)$) y direction, and define the rescaled adaptive deformation Global Linear Bending (ramGLB) deformation along a line parallel to the y axis as follows:

$$X_{ram} = r_x(z)X_{am} \quad (8)$$

$$Y_{ram} = r_y(z)\tilde{Y}_{am} + \tilde{y}_{am} \quad (9)$$

$$Z_{ram} = Z_{am} \quad (10)$$

where the X_{am} , Y_{am} , and Z_{am} denote the amGLB transformed x , y , and z coordinates. To define the rescaling factors, we define points $A(z) = (x_A, y_A, z)$, $B(z) = (x_B, y_B, z)$, and $C(z) = (x_C, y_C, z)$, where x_A, x_B are parameters whose meaning will be explained shortly and y_A, y_C are as in Eqs. (1) - (7), as functions of z -coordinate. Let $X_{am}(I, z)$, $Y_{am}(I, z)$, $I = A, B, C$ denote the x and y coordinates of these points after amGLB

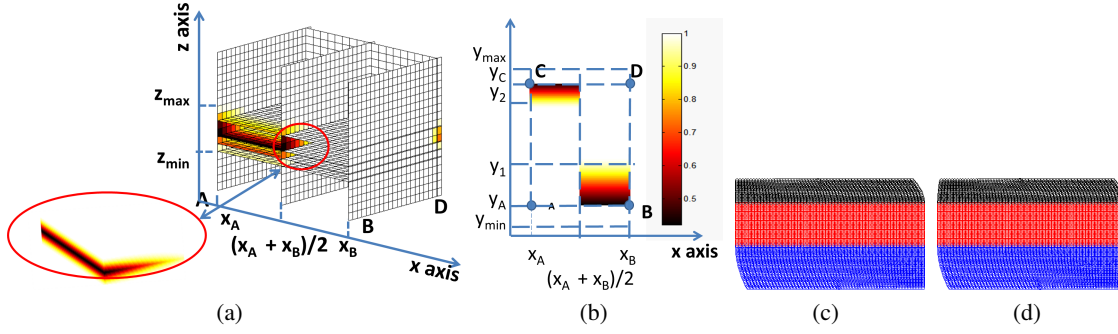


Figure 5: The rescaling factors of the rescaled adaptive modified Global Linear Bending (ramGLB). In (a) and (b) is shown the rescaling field factor along the x axis to be used in the ramGLB space remapping and in (d) the resulting ramGLB deformed space. We found experimentally that better results were achieved by adding the mean terms in the expression of the rescaling factor along x than in the case this additive mean terms were not used (c).

deformation. Then,

$$r_x(z) = \begin{cases} \frac{x_B - x_A}{X_{am}(A, z) - X_{am}(z, -\theta)} + \frac{x_A + X_{am}(A, z)}{2} & \text{if } x \geq \frac{x_B - x_A}{2}, y \leq y_1(z), z_{min} \leq z \leq z_{max} \\ \frac{x_B - x_A}{X_{am}(B, z) - X_{am}(z, -\theta)} + \frac{x_A + X_{am}(B, z)}{2} & \text{if } x < \frac{x_B - x_A}{2}, y \geq y_2(z), z_{min} \leq z \leq z_{max} \\ 1 & \text{otherwise} \end{cases} \quad (11)$$

$$r_y(z) = \begin{cases} \frac{y_A - y_1(z)}{Y_{am}(A, z) - y_1(z)} & \text{if } y \leq y_1(z), z_{min} \leq z \leq z_{max} \\ \frac{y_C - y_2(z)}{Y_{am}(C, z) - y_2(z)} & \text{if } y \geq y_2(z), z_{min} \leq z \leq z_{max} \\ 1 & \text{otherwise} \end{cases} \quad (12)$$

where $X_{ma}(A, z, -\theta)$ denotes the value of $X_{ma}(A, z)$ at point A in case of the flipping the sign of θ in Eq. (4). The rescaling in the x direction is designed to produce a rightwards bending of the portion of the space corresponding to the left occipital lobe ($y \leq y_1(z)$, $x \leq (x_B - x_A)/2$, here the rescaling factor along the x axis is 1), while at the same time resizing the portion of the space corresponding to the right occipital ($y \leq y_1(z)$, $x \geq (x_B - x_A)/2$) lobe (see Fig. 5). With these rescalings, we can synthesize the protrusion of the left occipital lobe over the right, while not deforming the exterior regions (e.g. skull) to the right occipital lobe. The rescaling along the y direction follows a similar idea for the image space corresponding to the right temporal lobe.

4 APPLICATION TO BRAIN IMAGING

Our motivation for studying the global bending deformations originated from a need to develop a simple, global model for the brain torque. Based on this

model given in previous section, we can introduce a known amount of realistic asymmetry to any given brain MR image, and therefore, construct a set of images with a known and easily parametrized asymmetry pattern. This dataset can be used for the quantitative validation of voxel level and surface based morphometric methods of brain shape asymmetry. This section describes an automatic image pipeline to generate such a dataset.

First, two artificially symmetrized images are obtained from each MR image. Next, the synthetic images are deformed by a customized model of the brain torque. In order to make sure that the parametric global linear bending deformation would produce a consistent level of bending deformations among images (despite of the eventually different image and voxel sizes), the deformation is applied to each synthetic image in stereotactic space and the deformed volumes are then registered back to the native space. All the image registration stages of the pipeline are performed using the FLIRT tool (Jenkinson and Smith, 2001) of the FMRIB FSL Software Library (<http://www.fmrib.ox.ac.uk/fsl/>). The pipeline workflow is depicted in Fig. 6 and described in the following 6 consecutive steps.

STEP 1: Image pre-processing. Each T1-weighted MR image is corrected for intensity non-uniformity (also referred as bias field) using a multi-resolution approach with a minimum intensity-gradient entropy criteria (Manjón et al., 2007). The bias field corrected images are denoised using a non-local means denoising algorithm which automatically adapts to the spatially varying noise levels of the MR images (Manjón et al., 2010).

STEP 2: Symmetrized images generation. The Left-Left (LL) and the Right-Right (RR) artificially symmetrized images are extracted from the pre-processed images. Each LL image is generated by replacing the right hemisphere (voxels on the

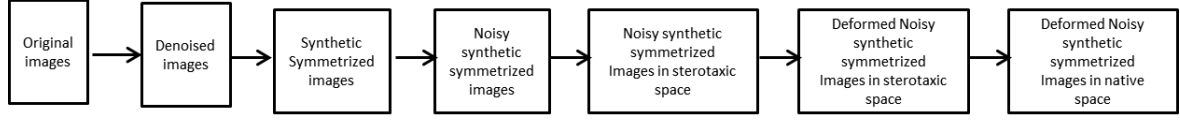


Figure 6: The proposed automatic image processing pipeline for the generation of a dataset for quantitative validation of morphometric methods for studying brain asymmetry from T1- weighted 3D MR images.

right hand side of the mid-sagittal plane) of the pre-processed image with the flipped version of the left hemisphere. The synthetic RR images are created in a similar way. If the original image exhibits an appreciable leftward (rightwards) asymmetry, than the LL (RR) image is discarded as a non realistic double inter-hemispheric fissure would appear along the inter-hemispheric plane in the regions of higher degree of right (left) hemisphere protrusion.

STEP 3: Addition of Rician noise. In MRI, measurement noise can be considered to be Rician distributed (Gudbjartsson and Patz, 1995). In order to create images with non-symmetric noise realizations, we add Rician noise to the denoised, symmetrized images.

STEP 4: Spatial normalization. The synthetic symmetrical LL and RR images are spatially normalized to symmetrical subject- and image- specific template images using affine registration. Affine registration parameters are estimated from the skull and scalp stripped synthetic symmetrical images and applied then to the corresponding non skull stripped synthetic symmetrical images. The skull stripping is performed by the Brain Extraction Tool (BET) (Smith, 2002) with default parameters. The above mentioned symmetrized subject- and image- specific template images are obtained for each synthetic image by first averaging it with its flipped version around the x axis. Next, the resulting average image is registered to the stereotaxic space ($181 \times 218 \times 181$ voxels of size $1.0 \times 1.0 \times 1.0 \text{ mm}^3$) using a 7 parameter affine transformation. By construction, these template images are symmetrical and registered to the stereotaxic space.

STEP 5: Volume deformations. The non skull stripped phantom images in stereotaxic space are deformed by the ramGLB deformation with the following model parameters: $k_1 = 0.00003$, $k_2 = -0.0001$, $n_{max} = 10$, $y_A = -90$, $y_1 = -22$, $y_2 = 62$, $y_C = 91$, $z_1 = 74$, $z_2 = 76$, $z_{min} = 45$ and $z_{max} = 105$. Indeed, for MR images in the stereotaxic space, we found experimentally that a realistic modeling of the inter-hemispheric fissure bending can be obtained by remapping the sub-space with $z \in [45, 105]$ while the remaining space was kept unchanged.

The modeling of more (less) intense patterns of the

inter-hemispheric bending at the occipital and frontal lobes could be easily achieved e.g. by increasing (decreasing) the $|k_1|$ and $|k_2|$ values. A realistic modeling of a typical pattern of inverted brain torque can also be obtained by the ramGLB space deformation with the following model parameters: $k_1 = -0.000015$, $k_2 = -0.0001$, $n_{max} = 10$, $y_A = -90$, $y_1 = -22$, $y_2 = 62$, $y_C = 91$, $z_{min} = 45$ and $z_{max} = 105$.

STEP 6: Back to the native space. The 7-parameter affine registration matrix used in step 4 is inverted and applied to the deformed synthetic images computed in step 5. As a result, the deformed synthetic images are mapped back to their native spaces.

The ramGLB-like deformation was applied to a dataset previously described in (Laakso et al., 2001) consisting of 19 T1-weighted MR images of right-handed healthy controls (7 females, 12 males). Results were visually inspected to verify that the deformed synthetic images were modeling a realistic rightward bending of the interhemispheric fissure as well as the hemispheric protrusions of the right occipital and left frontal lobes. A few examples of deformed synthetic images are depicted in Fig. 7. Particularly, Fig. 7 shows how well the images processed by the proposed image processing pipeline resemble the brain torque in the corresponding original MR images.

5 CONCLUSIONS

In this work, we have proposed space deformation methods to approximate the bending deformation in 3D volumes and surfaces, which add flexibility to the current SD methods for global bending. Particularly, the ramGLB was developed for the modeling of the inter-hemispheric bending of the human brain. The ramGLB space deformation can introduce a known amount of realistic asymmetry to any given 3D T1-weighted brain MR image. Due to the simplicity of the model and to the automatism of the whole image processing pipeline, the latter can be used for the quantitative validation of voxel and surface based morphometric methods for the study of the brain asymmetry in large databases. The proposed image processing pipeline was designed and tested for 3D T1-weighted MR images although it can be easily adapted for other structural imaging modalities.

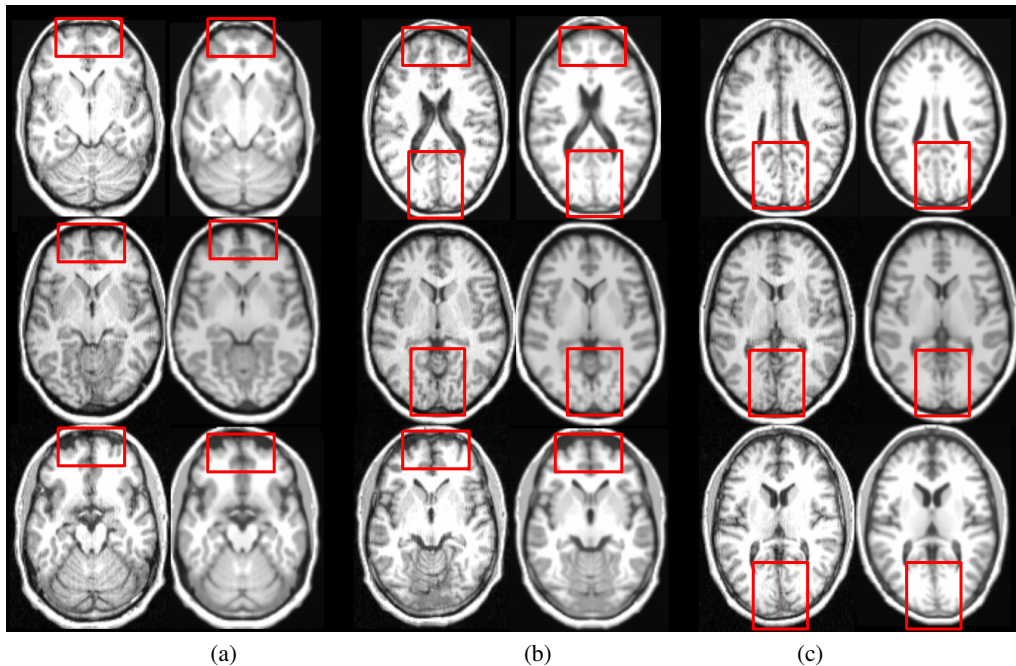


Figure 7: The original (left) T1-weighted MR images of three subjects (rows) are modified with the developed image processing pipeline (right). For each subject, three transversal views are shown (a)-(c). Synthesized images on right appear remarkably similar to the original images, but their asymmetry pattern is known exactly.

ACKNOWLEDGEMENTS This work was supported by the Academy of Finland grants 130275 and 129657, Finnish Programme for Centres of Excellence in Research 2006-2011).

REFERENCES

- Ashburner, J. and Friston, K. J. (2000). Voxel-based morphometry: the methods. *NeuroImage* 11(6), 805-821.
- Barr, A. (1984). Global and local deformations of solid primitives. *SIGGRAPH Comput. Graph.* 18(3), 21-30.
- Good, C., Johnsrude, I., Ashburner, J., Henson, R. N., Friston, K. J., and Frackowiak, R. S. (2001). Cerebral asymmetry and the effects of sex and handedness on brain structure: A voxel-based morphometric analysis of 465 normal adult human brains. *NeuroImage* 14 (3), 685 – 700.
- Gudbjartsson, H. and Patz, S. (1995). The rician distribution of noisy MRI data. *Magn. Reson. Med.* 34, 910-914.
- Hsu, W. (1992). Direct manipulation of free form deformations. *Comput. Graph.* 26(2), 176-182.
- Jenkinson, M. and Smith, S. M. (2001). A global optimisation method for robust affine registration of brain images. *Med. Image Anal.* 5(2), 143-156.
- Laakso, M. P., Tiihonen, J., Syvälahti, E., Vilkmann, H., Laakso, A., Alakare, B., Rääkkäläinen, V., Salokangas, R. K., Koivisto, E., and Hietala, J. (2001). A morphometric mri study of the hippocampus in first-episode, neuroleptic-naïve schizophrenia. *Schizophr. Res.* 50 (1-2), 3 – 7.
- Manjón, J., Coupé, P., Martí-bonmatí, L., Robles, M., and Collins, D. (2010). Adaptive non-local means denoising of mr images with spatially varying noise levels. *J. of Magn. Reson. Imaging* 31, 192-203.
- Manjón, J., Lull, J. J., Carbonell-Caballero, J., García-Martí, G., Martí-Bonmatí, L., and Robles, M. (2007). A nonparametric mri inhomogeneity correction method. *Med. Image Anal.* 11(4), 336-345.
- Pepe, A., Zhao, L., Tohka, J., Koikkalainen, J., Hietala, J., and Ruotsalainen, U. (2011). Automatic statistical shape analysis of local cerebral asymmetry in 3d t1-weighted magnetic resonance images. In *MICCAI 2011 MedMesh workshop*, 127 - 133.
- Sederberg, T. and Parry, S. (1990). Free form deformation of solid geometric models. *Comput. Graph.* 24(4), 151-1600.
- Smith, S. (2002). Fast robust automated brain extraction. *Hum. Brain Map.* 17(3), 143-155.
- Sumner, R. (2005). Mesh modification using deformation gradients. *Thesis (Ph. D.)—Massachusetts Institute of Technology*, 2005.
- Thompson, P. M., MacDonald, D., Mega, M. S., Holmes, C. J., Evans, A. C., and Toga, A. W. (1997). Detection and mapping of abnormal brain structure with a probabilistic atlas of cortical surfaces. *J. Comput. Assist. Tomo.* 21, 4 (1997), 567- 581.
- Toga, A. W. and Thompson, P. M. (2003). Mapping brain asymmetry. *Nat. Rev. Neurosci.* 4(1), 37-48.
- Xiaogang, J., Huagen, W., and Qunsheng, P. (2001). Geometric deformations based on 3d volume morphing. *J. Comput. Sci. and Technol.* 16(5), 443-449.